




# Tidally-induced nonlinear resonances in EMRIs with an analogue model

David Bronicki <sup>1,\*</sup> Alejandro Cárdenas-Avedaño <sup>2,3,4</sup> and Leo C. Stein <sup>1</sup>

<sup>1</sup>*Department of Physics and Astronomy, The University of Mississippi, University, Mississippi 38677, USA*

<sup>2</sup>*Programa de Matemática, Fundación Universitaria Konrad Lorenz, 110231 Bogotá, Colombia*

<sup>3</sup>*Illinois Center for Advanced Studies of the Universe,*

*University of Illinois at Urbana-Champaign, Urbana, Illinois 61801, USA*

<sup>4</sup>*Department of Physics, Princeton University, Princeton, NJ, 08544, USA*

(Dated: November 25, 2024)

One of the important classes of targets for the future space-based gravitational wave observatory LISA is extreme mass ratio inspirals (EMRIs), where long and accurate waveform modeling is necessary for detection and characterization. When modeling the dynamics of an EMRI, several effects need to be included, such as the modifications caused by an external tidal field. The effects of such perturbations will generally break integrability at resonance, and can produce significant dephasing from an unperturbed system. In this paper, we use a Newtonian analogue of a Kerr black hole to study the effect of an external tidal field on the dynamics and the gravitational waveform. We have developed a numerical framework that takes advantage of the integrability of the background system to evolve it with a symplectic splitting integrator, and compute approximate gravitational waveforms to estimate the time scale over which the perturbation affects the dynamics. We find that different entry points into the resonance in phase-space can produce substantially different dynamics. Finally, by comparing this time scale with the inspiral time, we find tidal effects will need to be included when modeling EMRI gravitational waves when  $\varepsilon \gtrsim 300 q^2$ , where  $q$  is the small mass ratio, and  $\varepsilon$  measures the strength of the external tidal field.

## I. INTRODUCTION

Future space-based detectors, such as the Laser Interferometer Space Antenna (LISA) [1], will allow studies of the gravitational waves (GWs) emitted when a small compact object, with mass  $m$ , falls into a supermassive one, with mass  $M$ , in an extreme mass-ratio inspiral (EMRIs), i.e., satisfying  $q = m/M \ll 1$ . EMRIs emit GWs in wavelengths inaccessible to ground-based detectors, such as the LIGO/Virgo/KAGRA detectors. They are expected to happen rarely in any one galaxy, but nevertheless thought to occur within the lifetime of the LISA mission [2, 3].

Generic EMRI orbits, which to zeroth order are bound Kerr geodesics, can be highly eccentric and inclined, and therefore the emitted GWs are expected to encode a rich phenomenology [4]. Geodesic motion in Kerr is integrable [5], so a bound Kerr orbit lies on a phase-space torus characterized by three frequencies: one each associated with the radial, polar, and axial motion [6, 7]. This torus is ergodically filled for most trajectories, but not for the resonant ones, i.e., when two frequencies form a co-prime low-integer ratio.

When a system is Liouville integrable [8], i.e., there are the same number of degrees of freedom as independent Poisson-commuting integrals of motion (such as geodesics in Kerr), the dynamics around resonances does not show a distinctive character. However, in the presence of a generic perturbation, there can be qualitative changes to phase space. From the KAM theorem [9], for sufficiently small perturbations, almost all non-resonant tori are deformed

but continue to foliate phase space. Meanwhile, close to resonant tori, we expect nonlinear resonances and chaos to develop.

Beyond the test-particle approximation, the dynamics deviate from geodesic motion due to a force arising from the gravitational field generated by the small particle. That perturbation is known as the particle’s self-force [10, 11] and generates dissipative (e.g., the radiation-reaction force) and conservative effects (e.g., the advance of the pericenter angle each orbit). The formative work on EMRIs was performed under the so-called “adiabatic” approximation [12], in which radiation reaction effects are torus-averaged to compute the inspiral. This procedure is well-justified for most trajectories [13] but fails at resonances [14]. Near resonances, the effects of perturbations are boosted (relative to their non-resonant size) by an amount inversely proportional to the square root of the mass ratio, and cause the system to evolve rapidly, or “jump,” from one adiabatic orbit to another [14, 15].

A “jump” can also arise from the conservative sector of the dynamics [16–19], at the level of the geodesic of a non-integrable system. Within the adiabatic approximation, prolonged resonances have been shown to appear [16, 19], that are expected to translate to “glitches” in the GW frequency [19].

Resonant effects can also be induced by the tidal field of nearby stars or stellar-mass black holes, a dark matter distribution, or the rest of the galactic potential [20, 21]. These tidal resonances will cause a secular shift to the orbital angular momentum, that, if properly modeled, would provide information about the distribution of mass near a galactic-center black hole [21]. Due to the intrinsic complexity and sources of resonant effects, a generic description is still lacking, and assessing the importance

\* [dbronick@go.olemiss.edu](mailto:dbronick@go.olemiss.edu)

of resonant effects on future gravitational detections with LISA has proven difficult [22, 23].

In this work, we carry out an approximate analysis that highlights important features of the resonant phenomena that should be taken into account when modeling EMRIs. To this end, we study a Newtonian Kerr “analogue” [24–26] and add a tidal perturbation. The analogue system is Euler’s 18th century problem of two fixed gravitating centers [24], which is the unique stationary and axisymmetric Newtonian potential that shares several key properties of the Kerr metric [25]. In particular, it is integrable, and has the same recurrence relation for the mass multipole moments [25, 26].

We found that this analogue is a good compromise between a system complex enough to exhibit resonant effects, and still simple enough to be numerically and analytically tractable. After numerically evolving trajectories of the perturbed system, computing approximate gravitational waveforms, and performing an analysis of dephasing times, we estimate a region of parameter space for which the characteristic timescale of the tidal perturbation at resonance is shorter than the inspiral time. That is, we estimate a range of parameter space where a proper modeling of the tidal perturbation is necessary to properly model the waveform. We also found that the different entry points into the resonance in phase space can produce substantially different dynamics.

The remainder of this paper shows the details of the calculations that led to the above conclusions. In Sec. II we give an overview of the Newtonian analogue, and in Sec. III we present how it is tidally perturbed. Our numerical scheme is presented in Sec. IV. We characterize the resonant dynamics in Sec. V, before studying the approximate gravitational waves in Sec. VI. Finally in Sec. VII we present our conclusions and perspectives. Throughout the paper we use geometric units in which  $G_N = c = 1$ , and set  $M = 1$  for all our numerical implementations.

## II. A NEWTONIAN ANALOGUE TO THE KERR SPACETIME

The system we study in this work is a particle moving in the oblate version of Euler’s potential of two fixed centers [24]. In this section, we give a brief summary of the system and only the equations directly required for our purposes. For a more complete description of the system, see Refs. [24–26].

The gravitational potential is generated by two fixed point particles with some separation  $2a$ . To make the system analogous to the Kerr spacetime, the masses of both particles are set to  $M/2$  (making the potential parity symmetric) and an oblate characteristic is enforced by setting the separation to an imaginary value  $2ia$  [24, 27]. Upon making the further choice of aligning the separation with the  $z$  axis, the potential can be expressed as

$$V = -\frac{M}{R^2\sqrt{2}}\sqrt{R^2 + r^2 - a^2}, \quad (1)$$

where  $R \equiv \sqrt{(r^2 - a^2)^2 + 4a^2z^2} = r_a r_b$ , and  $r_a$  and  $r_b$  are the distances from each fixed mass.

In the analogy to the Kerr spacetime,  $M$  and  $a$  are analogous to the mass and spin of the black hole, respectively. In addition, this analogue is endowed with a third independent commuting constant of motion, and thus, it is completely integrable [24], as is the Kerr spacetime. The motion can be separated in oblate spheroidal coordinates with

$$\begin{aligned} \text{radial-like coordinate:} & \quad r = a\xi \in [0, \infty) \\ \text{polar-like coordinate:} & \quad \cos\theta = \eta \in [-1, 1] \\ \text{azimuthal coordinate:} & \quad \phi \in [0, 2\pi) \end{aligned} \quad (2)$$

related to cylindrical coordinates by

$$\begin{aligned} \rho &= a\sqrt{1 + \xi^2}\sqrt{1 - \eta^2} \\ z &= a\xi\eta. \end{aligned} \quad (3)$$

Since we are considering motion to be that of a test mass, we work with quantities per unit test mass, i.e.,  $p = P/m$  and  $H = E/m$ , where  $P$  and  $E$  are the standard momenta and energy. In particular, the momenta relate to the above coordinates by

$$\begin{aligned} p_\xi &= a^2 \left( \frac{\xi^2 + \eta^2}{1 + \xi^2} \right) \dot{\xi}, \\ p_\eta &= a^2 \left( \frac{\xi^2 + \eta^2}{1 - \eta^2} \right) \dot{\eta}, \\ p_\phi &= a^2(1 + \xi^2)(1 - \eta^2)\dot{\phi}, \end{aligned} \quad (4)$$

and the Hamiltonian is

$$\begin{aligned} H &= \frac{p_\xi^2}{2a^2} \frac{1 + \xi^2}{\xi^2 + \eta^2} + \frac{p_\eta^2}{2a^2} \frac{1 - \eta^2}{\xi^2 + \eta^2} \\ &+ \frac{p_\phi^2}{2a^2} \frac{1}{(1 + \xi^2)(1 - \eta^2)} - \frac{M\xi}{a(\xi^2 + \eta^2)}. \end{aligned} \quad (5)$$

As two coordinates do not appear in the Hamiltonian, we have two immediate conserved quantities: from the time symmetry we have  $H = \text{const.}$ , and from the axial symmetry we have  $\ell := p_\phi = \text{const.}$  The Hamilton-Jacobi theory can be implemented to further separate the system and obtain the third and final independent conserved quantity:

$$\begin{aligned} \beta &= -2a^2H(1 + \xi^2) + p_\xi^2(1 + \xi^2) - \frac{\ell^2}{1 + \xi^2} - 2aM\xi \\ &= -2a^2H(1 - \eta^2) - p_\eta^2(1 - \eta^2) - \frac{\ell^2}{1 - \eta^2}. \end{aligned} \quad (6)$$

Following this separation, new expressions for the momenta arise:

$$\begin{aligned} p_\xi &= \pm \sqrt{\frac{2a^2H(1 + \xi^2) + \frac{\ell^2}{1 + \xi^2} + 2aM\xi + \beta}{1 + \xi^2}} \\ &= \frac{\pm 1}{1 + \xi^2} \sqrt{P_\xi(H, \ell, \beta; \xi)} \end{aligned}$$

and

$$p_\eta = \pm \sqrt{\frac{-2a^2 H(1-\eta^2) - \frac{\ell^2}{1-\eta^2} - \beta}{1-\eta^2}} \\ = \frac{\pm 1}{1-\eta^2} \sqrt{P_\eta(H, \ell, \beta; \eta)}, \quad (7)$$

where  $P_\xi$  and  $P_\eta$  are fourth order polynomials in  $\xi$  and  $\eta$ , respectively.

In studying the motion of particles in bound orbits, the previous two equations become quite important. By requiring the arguments of the radicals to be positive (so as to have real-valued momenta), we see that the motion in  $\xi$  and  $\eta$  becomes constrained to be between the roots of  $P_\xi$  and  $P_\eta$  respectively. To sit above the separatrix (analogous to requiring we not sit in a plunging orbit), we assign  $\xi_1 = r_1/a$  and  $\xi_2 = r_2/a$  to be the largest and second largest roots of  $P_\xi$ . The other two roots may be real or complex. For motion along the polar coordinate, we define  $\eta_{\max}$  to be the smallest positive root of  $P_\eta$ .  $P_\eta$  is a biquadratic, so  $-\eta_{\max}$  is also a zero and is the lower turning point. The other roots of  $P_\eta$  are also symmetric to one another and must both be real. The set of turning points  $(r_1, r_2, \eta_{\max})$  constitute an alternative set of constants of motion. To relate these constants to more traditional Keplerian style orbital constants, we define eccentricity  $e$ , semilatus rectum  $p$ , and inclination  $I$  such that

$$r_1 = \frac{p}{1-e}, \quad r_2 = \frac{p}{1+e}, \quad \sin I = \eta_{\max}. \quad (8)$$

As in the Kerr solution, the radial and polar coordinates are not periodic functions of the proper time [6]. However, when expressed in Mino time [28], the equations of motion separate further and periodicity becomes manifest. Following this insight, as found in Ref. [26], the equations of motion become

$$\frac{d\xi}{d\lambda} = \pm \sqrt{P_\xi(\xi)} \quad \frac{d\phi}{d\lambda} = \ell \left[ \frac{1}{1-\eta^2} - \frac{1}{1+\xi^2} \right] \\ \frac{d\eta}{d\lambda} = \pm \sqrt{P_\eta(\eta)} \quad \frac{dt}{d\lambda} = a^2(\xi^2 + \eta^2). \quad (9)$$

The last equation here is the defining relation of Mino-like time,  $\lambda$ .

We note that the fundamental frequencies of the system can be found analytically. By considering the equations of motion directly, these fundamental frequencies are derived in Appendix E of Ref. [26]. We will make use of these frequencies in Sec. VI.

### III. TIDAL PERTURBATION

We now consider the effect of an additional gravitating body or a congregate gravitational potential. This perturbing potential can for example arise from a nearby

supermassive black hole, a star orbiting the primary outside the orbit of the secondary, or an overall galactic potential due to nearby stars and dark matter. In general relativity, the local effects of gravity – such as an external tidal field – can be modeled by using Riemann normal coordinates [29]; the dominant effect is captured by the electric part of the Riemann tensor,

$$E_{ij} = R_{0i0j}, \quad (10)$$

where  $R_{\mu\nu\rho\sigma}$  is the Riemann curvature tensor. Meanwhile in Newtonian gravity, we may Taylor expand an external gravitational potential about the origin as

$$V_{\text{ext}} = V_0 + V_j x^j + \frac{1}{2} V_{jk} x^j x^k + O(x^3). \quad (11)$$

The first term is a constant and is removed by redefining zero energy. The second, linear, term results in a constant force on both the central body and the test particle equally, and can be removed by choosing a freely falling frame for the binary. This leaves, to lowest order,

$$V_{\text{ext}} = \frac{1}{2} V_{ij} x^i x^j. \quad (12)$$

Although  $V_{ij}$  may in general depend on time, we will consider no time dependence for simplicity.

Note that in our units,  $H = E/m$  (and by extension  $V$  and  $V_{\text{ext}}$ ) is dimensionless. Since  $x_i$  has dimensions of mass,  $V_{ij} = \partial_i \partial_j V_{\text{ext}}$  has units of  $1/M^2$ . We will define  $\varepsilon$  and  $A_{ij}$  such that  $V_{ij} = \varepsilon A_{ij}/M^2$ , where  $M$  is the mass of the central body,  $A_{ij}$  is dimensionless and order unity, and we capture the smallness of the external tidal field by  $\varepsilon \ll 1$ . Eq. (12) now becomes

$$V_{\text{ext}} = \frac{1}{2} \varepsilon A_{ij} \frac{x^i x^j}{M M}. \quad (13)$$

If the tidal force is due to a gravitating body of mass  $M_*$  at a distance  $d$  from the center of the system, then

$$\varepsilon \sim \frac{M^2 M_*}{d^3}. \quad (14)$$

As an illustrative case, consider the environment in the center of our own galaxy, where we have a BH with mass  $M = M_{\text{Sgr A}^*} \sim 4 \times 10^6 M_\odot$ , expected to be surrounded by a population of stellar-mass black holes  $M_* \sim 40 M_\odot$  with a mean distance of  $d \sim 7.5 \times 10^{11}$  meters [30]. With these values, the tidal strength is  $\varepsilon \sim 5 \times 10^{-12}$ . We can also consider a system in which the primary is a supermassive black hole with  $M = 10^9 M_\odot$ , and is perturbed by another supermassive black hole, with  $M_* = 10^6 M_\odot$ . By considering the perturber to be near by with  $d \sim 4 \times 10^{13}$  meters, e.g., during the late stages of the merger of galaxies, we find a stronger perturbation amplitude of  $\varepsilon \sim 5 \times 10^{-8}$ .

As the detection rates and specifics of these different types of systems are subject to several uncertainties [1, 3, 20], for our analysis we consider cases with perturbation amplitudes in the range  $\varepsilon \in [10^{-9}, 10^{-5}]$ . Furthermore,

to reduce the parameters modeled, we make the arbitrary, symmetry-breaking choice of

$$A = \begin{bmatrix} 1.2 & 1.3 & 1.2 \\ 1.3 & 1.3 & 1.2 \\ 1.2 & 1.2 & -2.5 \end{bmatrix}. \quad (15)$$

Our results are independent of the choice of these numbers, provided that the constraints of symmetric and trace free are satisfied, these number are of order unity, and that there is no accidental symmetry (such as axial symmetry).

#### IV. SYSTEM INTEGRATION ALGORITHM

Due to its desirable properties for long-duration integration, we implement a symplectic splitting integrator [31] to evolve the system. As such, we split the Hamiltonian into

$$H = H_0 + V_{\text{ext}} \quad (16)$$

where  $H_0$  was discussed in Sec. II and  $V_{\text{ext}}$  was discussed in Sec. III. For a generic symplectic splitting method [31], the system state  $(x, p)$  is evolved under  $H$  by the scheme

$$\begin{aligned} \exp(\Delta t D_H)(x, p) &= \exp(a_1 \Delta t D_{V_{\text{ext}}}) \exp(b_1 \Delta t D_{H_0}) \cdots \\ &\exp(a_N \Delta t D_{V_{\text{ext}}}) \exp(b_N \Delta t D_{H_0})(x, p) + \text{error}, \end{aligned} \quad (17)$$

where the infinitesimal time evolution operator is

$$D_H \cdot = \{\cdot, H\}. \quad (18)$$

We require the coefficients to be constrained by

$$\sum a_i = \sum b_i = 1, \quad (19)$$

so that over one step the system is evolved a total of  $\Delta t$  through both  $H_0$  and  $V$ . As with all numerical techniques, the order of accuracy depends on the number of stages used and the coefficients ( $a_i$  and  $b_i$ ). In our case, we use

$$\begin{aligned} a_1 &= 1/4 & b_1 &= 2/3 \\ a_2 &= 3/4 & b_2 &= 1/3. \end{aligned} \quad (20)$$

This choice produces an algorithm accurate to third order in time step and to first order in perturbation magnitude. That is, our error terms are all of the form

$$\text{error} = O(\varepsilon^i \Delta t^j), \quad (21)$$

where either  $i \geq 2$  or  $j \geq 4$ .

Equation (17) assumes exact or near exact methods exists to integrate each subsystem  $H_0$  and  $V_{\text{ext}}$ . While  $H_0$  can in principle be expressed analytically by relating the coordinates at time  $t$  to those at time  $t + b_i \Delta t$  with elliptic integrals, it is far simpler to numerically evolve the separated system in adapted coordinates. The precise

numerical integrating method used to evolve each subsystem is not important; we chose to use the RK45 method of the `solve_ivp` routine provided by `scipy` [32].

This choice comes with a caveat, however. Since we intend to integrate through many orbits, the system will pass through many turning points. At each turning point, for instance at  $\xi_2$ , the relevant equation of motion is locally

$$\frac{d\xi}{d\lambda} \approx \pm A \sqrt{\xi - \xi_2}. \quad (22)$$

The issue here is twofold. First, the sign is ambiguous, and so care would have to be taken to keep track of which direction we travel and when this direction switches. Secondly, since the square root function has unbounded derivative, this system violates the Lipschitz condition for existence and uniqueness [33]. We therefore implement new angle-like coordinates  $\psi$  and  $\chi$  to replace  $\xi$  (or  $r$ ) and  $\eta$ , defined by

$$a\xi = r = \frac{p}{1 + e \cos \psi}, \quad \text{and} \quad \eta = \eta_{\text{max}} \cos \chi. \quad (23)$$

Unlike  $\xi$  and  $\eta$ ,  $\psi$  and  $\chi$  are monotonic, removing the sign issue. These definitions also analytically cancel the roots at the turning points; after a bit of algebra, their time derivatives satisfy the Lipschitz condition. In particular, the new equations of motion are

$$\begin{aligned} \frac{d\psi}{d\lambda} &= \frac{\sqrt{-2a^2 H \xi_1 \xi_2 (\xi^2 + b\xi + c)}}{\xi} \\ \frac{d\chi}{d\lambda} &= \sqrt{-2a^2 H (z_+ - \eta^2)} \end{aligned} \quad (24)$$

with

$$\begin{aligned} b &= \xi_1 + \xi_2 + \frac{1}{aH} \\ c &= (\xi_1 + \xi_2)b - \xi_1 \xi_2 + \frac{\beta}{2a^2 H} + 2, \end{aligned} \quad (25)$$

and  $z_+$  is the square of the upper root of  $P_\eta$ . Although the integration here is done with respect to Mino time  $\lambda$ , the integration is terminated once time  $t$  has advanced by  $b_i \Delta t$  so as to be consistent with the requirements of the symplectic integrator.

The integration under  $V_{\text{ext}}$  is far simpler since it is only a function of position and not momentum. In Cartesian coordinates, we have

$$\begin{aligned} \dot{x}_i &= \{x_i, V_{\text{ext}}\} = 0 \\ \dot{p}_i &= \{p_i, V_{\text{ext}}\} = -V_{ij} x^j. \end{aligned} \quad (26)$$

So  $x^i$  does not change, and  $p_i$  changes linearly with time (a ‘‘momentum kick’’). The new system state is then realized by re-evaluating the various ‘‘constants’’ of motion. Since this changes the turning points, the phase angles  $\chi$  and  $\psi$  must also be re-evaluated.

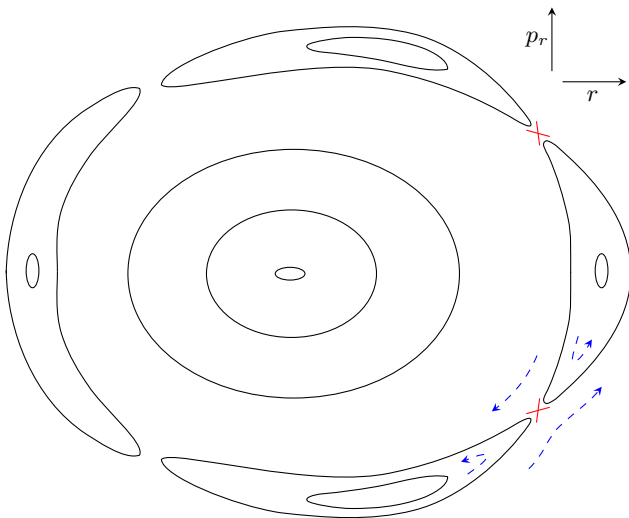


FIG. 1. A schematic diagram showing the characteristics of a Poincaré surface of section for a perturbed system. The inner circles, where the original torus structure is preserved, are far from resonance, while the outer circles show the breaking of a resonant torus into a nonlinear resonance, forming a “chain of islands.” The red crosses and blue flow lines show the hyperbolic points and the direction the system evolves under the Poincaré map near such points. The centers of the “islands” are elliptic points. With four elliptic points and four hyperbolic points, this diagram could correspond to a radial to polar frequency resonance of 1:4, 3:4, or 5:4, etc.

## V. DYNAMICS AT RESONANCE

In this section, we delve into the dynamics at resonance when under a tidal perturbation. To this end, we will discuss three core components: Poincaré sections, the KAM theorem, and resonance angles [9].

### A. Poincaré Sections

Let us briefly discuss a useful technique for graphically representing the behavior of the dynamical system. The graphical representation, known today as a Poincaré surface of sections or map of first recurrence [34], is obtained by considering the intersections of trajectories sharing the same value of energy with an arbitrary, but fixed, two-dimensional surface in phase space. Whenever the trajectory pierces the surface, the location in phase space is recorded, and the pattern generated on the surface constitutes the Poincaré surface of sections. The resulting figure, initially proposed by Poincaré, is extremely useful for systems of two degrees of freedom, as it is capable of providing a complete two-dimensional graphical representation of the four dimensional manifold, as sketched in Fig. 1. We describe its structure in the following section.

In our case, we choose the equatorial ( $xy$ ) plane as the surface that any bound orbit with a non-zero inclination will consistently intersect. With the further constraints

of accepting only ascending trajectories and  $H = \text{const.}$ , we are left with a four dimensional surface in phase space. Thus, the two dimensional representation originally conceived by Poincaré cannot accurately capture the behavior of the perturbed system, as it will be a projection. However, as pointed out in Ref. [35] if the fourth dimension is represented by a color variation (see Refs. [36–38] for some examples), all the dimensions can be visualized, to some degree, on a colored 3D plot. An example of such 4D space of section is shown in Fig. 2.

On the other hand, if we utilize the (approximate) exact azimuthal symmetry of the (perturbed) unperturbed case, we are able to further stipulate  $\ell = \text{const.}$  and safely ignore the azimuthal coordinate. This reduces our visual representation to a traditional two dimensional surface, as seen in Fig. 1 or in the  $r - p_r$  plane of Fig. 2.

### B. KAM Theorem

The Kolmogorov–Arnold–Moser (KAM) theorem [39] enters our discussion as it makes statements regarding integrable systems when perturbed. In particular, under a sufficiently small perturbation, quasi-periodicity is retained for almost all orbits, resulting in small deformations of the nested torus structure of integrable Hamiltonian systems. However, the theorem only guarantees this behavior for “sufficiently irrational” ratios of fundamental frequencies. Our interest is exactly at the resonant tori, with small-integer ratios of frequencies. We find, as is generally the case, that when sufficiently close to a resonance, the torus structure breaks completely. This break of structure constitutes a topological change, and can lead to both nonlinear resonances and chaos [39].

A cartoon of the structure of nonlinear resonances on a Poincaré section is shown in Fig. 1. The inner sections of the figure are far from resonance and so the nested torus structure is retained. A resonant torus of the unperturbed system has developed into a chain of “islands” of a single nonlinear resonance. Each island surrounds an elliptic fixed point, and they are separated by an equal number of hyperbolic fixed points (red crosses). In the nomenclature of [40], if an EMRI crossed such a nonlinear resonance, it would be called a “sustained” resonance, since two or more fundamental frequencies have an approximately constant ratio throughout the entire island.

The dynamics within the elliptic islands can be intuitively understood by drawing an analogy with a nonlinear pendulum (the pendulum analogy can be made even more precise in certain Solar system dynamics systems [41]). The pendulum’s degree of freedom is analogous to the slow oscillation of a Lissajous figure of the nonlinearly resonant trajectory. Approaching the elliptic fixed point, the amplitude of the oscillation decreases. The edge of the island is analogous to the separatrix of the pendulum’s motion — outside the island is the region where the pendulum rotates rather than oscillates. The analogy is strengthened in that the period of oscillation becomes

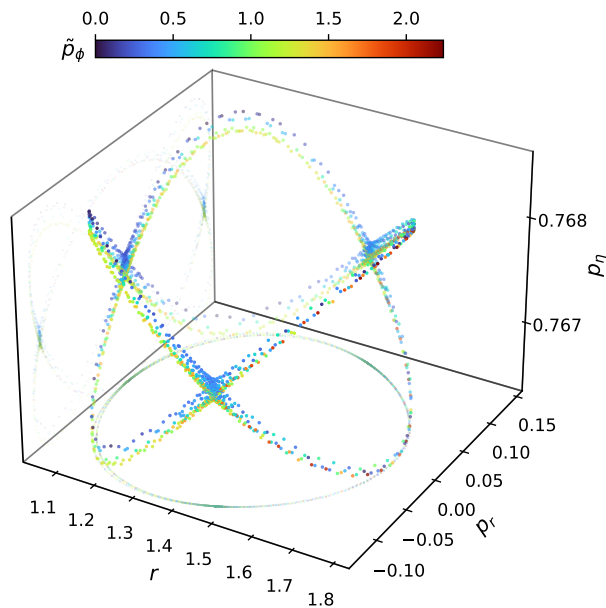


FIG. 2. A 4-dimensional Poincaré section for a perturbed system with  $\varepsilon = 10^{-5}$ , close to a nonlinear resonance. The colors correspond to the momentum associated with the coordinate  $\phi$ , which, for visualization purposes, has been scaled as  $\tilde{p}_\phi = 10^4(p_\phi - p_\phi^{\min})$ . The (minor) mixing of the colors indicates the presence of weakly chaotic orbits in the “sea” surrounding the quasiperiodic islands. A single orbit in this sea can pass close to a hyperbolic fixed point, hence the sea can completely surround the elliptic islands. The islands and surrounding sea are extremely narrow when projected onto the  $(r, p_r)$  plane, but it is apparent that the KAM curve has non-zero width.

amplitude-independent (like a simple harmonic oscillator) when approaching the elliptic fixed point, while the period diverges when approaching the separatrix.

A 2D projection, e.g., see the  $r - p_r$  plane in Fig. 2, does not necessarily distinguish whether or not the torus structure has broken [38]. Rather, it is the mixing of colors or the appearance of irregular behavior on the three-dimensional projection [35] which signals the breaking of a KAM torus. Thus, when studying the perturbed system, we first use the 3D colored projection to check that the trajectory belongs to a broken tori structure. Only once this is done can we be confident we have a non-linear resonance and move to using the 2D projection to study the dynamics more easily.

### C. Resonance Angles

When considering (orbital) dynamics at resonance, one finds by definition that two of the system’s phase angles evolve together with a specific rational ratio remaining approximately constant. As a result, one may define a “resonance angle” to be the difference of these phase angles with integer coefficients [41]. We will focus on a system

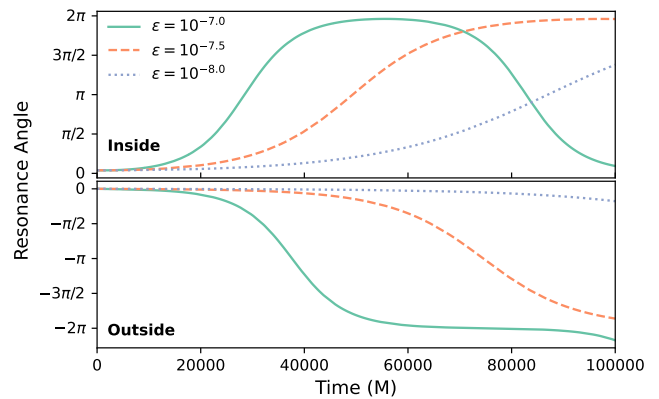


FIG. 3. Dynamics of the resonance angle  $\Psi$  inside the elliptic region and outside. Various levels of perturbation are shown for each plot. Inside the islands (upper panel) shows oscillatory motion, while the exterior (lower panel) shows rotating behavior, where  $\Psi$  grows without bound. We also note a shorter period of oscillation and faster rotation for larger perturbation amplitudes.

with a 2 : 3 polar to radial frequency resonance, that is,

$$\begin{aligned} \psi &\approx 3\omega_0 t + \psi_0 && \text{radial phase angle} \\ \chi &\approx 2\omega_0 t + \chi_0 && \text{polar phase angle} \\ \Psi := 3\chi - 2\psi &\approx \text{constant} && \text{resonance angle.} \end{aligned} \quad (27)$$

When a perturbation is applied, however, the phase angles will no longer evolve in such a simple fashion, and so non-trivial dynamical information can be garnered from the resonance angle. In Fig. 3, we show how the resonance angle evolves near resonance for various amplitudes of perturbation. We can see a qualitative difference between trajectories inside the elliptic region to those outside. As expected from the pendulum model, we observe oscillating behavior only inside.

To better explore the dynamics inside and outside of the elliptic region, we further specialize to a perturbation amplitude of  $\varepsilon = 10^{-7.5}$  and perform a sweep of trajectories with initial conditions in each category. A few samples of these sweeps are shown in Fig. 4. From these plots, we see that near the center of the elliptic region, trajectories become near perfect sinusoids, where the period is approximately amplitude-independent (the behavior of a simple harmonic oscillator). Far from the center, near the separatrix of the region, the orbits remain oscillatory, but with arbitrarily long periods (the behavior of a pendulum near its separatrix). Outside the region, we see the resonance angle “rotate,”  $\Psi$  monotonically decreasing or increasing with time, depending on what side of the hyperbolic point they sit.

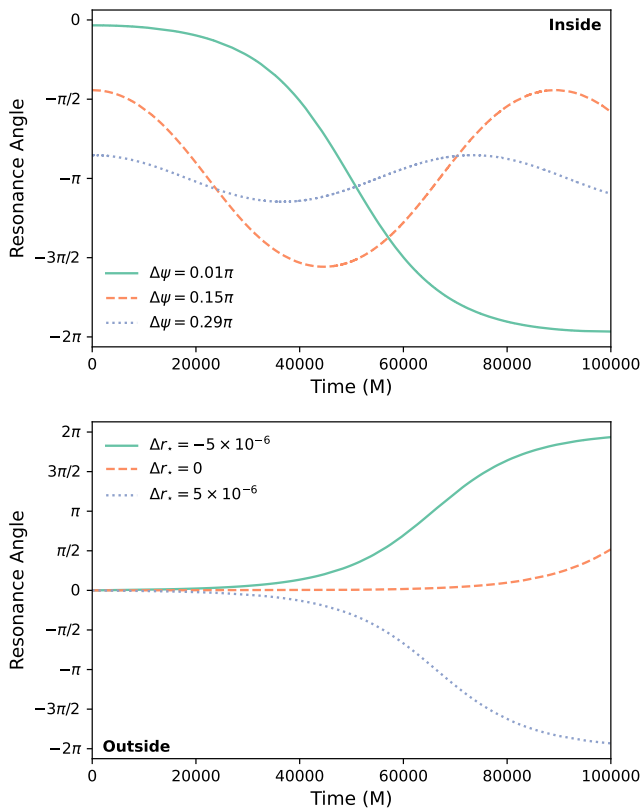


FIG. 4. Top: Inside the elliptic region. The blue dotted line is nearest to the elliptic fixed point while the green solid line is nearest to the separatrix and hyperbolic fixed point. Bottom: Outside the elliptic region. The orange dashed line is nearest to the separatrix and the hyperbolic fixed point.

## VI. APPROXIMATE GRAVITATIONAL WAVEFORMS

Equipped with an understanding of the dynamics at resonance for this system, we now turn to analyze the implications for detectability and modeling. For this purpose and neglecting gravitational wave dissipation, we construct kludge waveforms [42, 43] for the perturbed system and for the unperturbed system. We then consider the match between these to find whether or not it is necessary to model external tidal perturbations.

With our goals set in mind, several details must be handled. First, we must obtain the kludge waveforms from the phase space information we have. Second, we must find a consistent way to find pairs of systems, one perturbed and the other unperturbed, which can be identified together and compared via waveform match calculations. And finally, we must choose a figure of merit for determining how necessary is it to model tidal perturbations.

### A. Construction of Kludge Waveforms

We compute approximate gravitational waveforms closely following the procedure described in Refs. [42–44]. In this approach, the motion around the central black hole is interpreted as motion in flat spacetime, and gravitational waves are emitted as if in flat spacetime via a multipole decomposition [45].

These approximate waveforms, also known as “numerical kludges,” are defined as  $h = h_+ - ih_\times$ , where the two waveform polarizations (“plus” and the “cross”) are obtained from  $h_{+,\times} = \epsilon_{+,\times}^{ij} h_{ij}^{TT}/2$ . To lowest order, the metric perturbation in transverse-traceless gauge is

$$h_{ij}^{TT} = \left[ \frac{2}{R} I_{ij}^{(2)} + \frac{4}{3R} J_{k(i}^{(2)} \epsilon_{j)kl} \hat{n}_l \right]^{TT}, \quad (28)$$

with

$$\begin{aligned} I_{ij}^{(2)} &= m [(a_i x_j + 2v_i v_j + x_i a_j)]^{\text{STF}} \\ J_{ij}^{(2)} &= m [x_i (\vec{v} \times \vec{a})_j + 2v_i (\vec{x} \times \vec{a})_j \\ &\quad + x_i (\vec{x} \times \vec{j})_j + a_i (\vec{x} \times \vec{v})_j]^{\text{STF}}. \end{aligned} \quad (29)$$

In these expressions, STF denotes the symmetric-tracefree projection operator, TT is the transverse-traceless projection operator,  $R$  the flat-space distance from the source to the observer, and  $x_i(t)$  is the set of Cartesian components of the spatial trajectory of the small compact object. Under this approach, a trajectory is interpreted as if in flat space.

Since we work in a Newtonian analogue to Kerr spacetime, no reinterpretation is needed and we may use Eq. (3) to relate our phase-space variables to Cartesian coordinates. Furthermore, we can evaluate the velocity, acceleration, and jerk of the particle in Cartesian coordinates by evaluating  $v_i = \{x_i, H\}$ ,  $a_i = \{v_i, H\}$ , and  $j_i = \{a_i, H\}$ .

The polarization tensors  $\epsilon_{+,\times}^{ij}$  are built from an orthonormal triad with two components,  $p$  and  $q$ , chosen by the observer, and the third,  $n$ , in the direction of wave propagation. Explicitly, these polarization tensors are  $\epsilon_{+ij} = p_i p_j - q_i q_j$  and  $\epsilon_{\times ij} = 2p_{(i} q_{j)}$ . We use the most common triad, given in terms of the observation point’s latitude and azimuth,  $\Theta$  and  $\Phi$ , respectively, [43, 44] given explicitly by

$$\{n, p, q\} = \left\{ \frac{\partial}{\partial r}, \frac{1}{r} \frac{\partial}{\partial \Theta}, \frac{1}{r \sin \Theta} \frac{\partial}{\partial \Phi} \right\}. \quad (30)$$

We scale the resulting strain by setting  $R = 1$  and choose a polar angle of  $\Theta = \pi/6$  and azimuthal angle of  $\Phi = \pi/4$ .

Despite the approximations made during the generation of these waveforms, this procedure reproduces most of the features expected for EMRI sources and, for certain parameters, shows great agreement with more accurate Teukolsky-based waveforms [43, 46].

## B. Locating Comparable Trajectories

In the case of a real detection, a signal is received ( $h_{\text{obs}}$ ) and the best matching modeled signal is found ( $h_{\text{model}}$ ). We take the signal of the trajectory in a perturbed system to be the observed signal, and for the model we take the signal of an unperturbed system. We therefore first find a set of initial conditions  $\lambda_{\text{pert}}$  which are in the non-linear resonance for the perturbed system, and integrate them with  $H$  to obtain a waveform  $h_{\text{obs}}$ . We then seek a set of initial conditions  $\lambda_{\text{unpert}}$  for the unperturbed system which, once integrated with  $H_0$ , produce a waveform  $h_{\text{model}}$ , which maximizes the match with  $h_{\text{obs}}$ .

To the first task, we use the analytic expressions for fundamental frequencies found in Ref. [26] to find the radial to polar frequency ratio associated with any set of initial conditions. We then choose  $a = 0.7$ ,  $p = 1.3$ , and  $e = 0.25$ , and require  $f_\xi : f_\eta = 2 : 3$ . With this,  $\eta_{\text{max}}$  can be found numerically, giving  $\eta_{\text{max}} \approx 0.542$ . This places the system in resonance and, when perturbed, produces a non-linear resonance. With phase angles of  $\phi = 0$ ,  $\psi = \pi$ , and  $\chi = 0$ , we find trajectories near the hyperbolic point. To find the exact location of the hyperbolic point, we produced Poincaré sections spanning the hyperbolic point, and assessed the necessary initial conditions by eye. This hyperbolic point is then used as a jumping off point to analyzing trajectories inside the elliptic region, by adjusting the initial radial phase angle, or outside the elliptic region, by adjusting the turning point,  $r_2$ .

Ideally, finding the best matching set of unperturbed initial conditions  $\lambda_{\text{unpert}}$  would involve a full parameter search. This is, however, quite computationally expensive, due to each evaluation requiring a full integration of initial conditions. We therefore use the dynamical quantities of the perturbed system to make this process faster. We obtain the fundamental frequencies of the signal by considering the evolved phase coordinates as functions of time, and taking the slope of a linear fit. Intuitively, this is quite similar to taking

$$f_i^{\text{pert}} = \frac{\theta_i^{\text{final}} - \theta_i^{\text{initial}}}{\Delta t}. \quad (31)$$

We found this frequency extraction technique to perform better than a Fourier-based approach (as the one presented in, for instance, Ref. [16]). We then find best-fitting constants of motion by requiring the fundamental frequencies  $f_i^{\text{unpert}}$  to be the same as  $f_i^{\text{pert}}$ , and, as mentioned in Sec. II, we have analytic expressions for the frequencies.<sup>1</sup> We do not perform any search on the phase angles ( $\phi, \chi, \psi$ ), instead simply using the same initial phase angles.

<sup>1</sup> Notably, frequencies in Mino time will not do here. It is possible to find a system which agrees in all three frequencies in Mino time but which has a different average value for  $dt/d\lambda$  and therefore have different true frequencies.

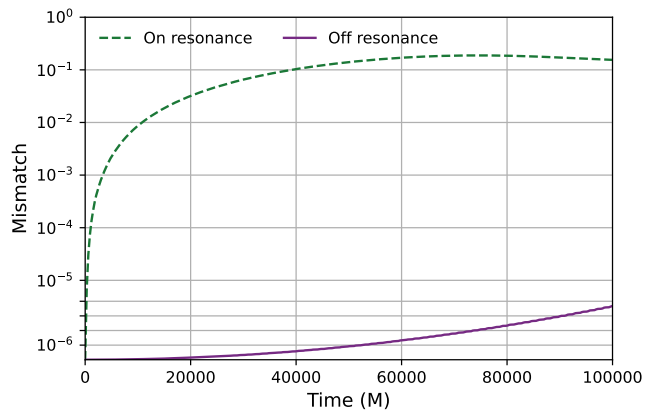


FIG. 5. Dephasing between perturbed and unperturbed orbits when in a nonlinear resonance and when far from resonance with  $\varepsilon = 10^{-8}$ . A linear scale is used near zero (in the finely segmented region) and a log scale is used elsewhere. Note that the off resonance mismatch does not exceed  $10^{-5}$ .

For any waveform generated from a perturbed system, we can now generate a nearby unperturbed waveform. If using an unperturbed system is a good approximation, then the match between the two waveforms should be quite high (or equivalently the mismatch quite low). Given two waveforms  $h_1$  and  $h_2$ , we use the fitting factor for match [47]:

$$FF(h_1, h_2) := \frac{\langle h_1 | h_2 \rangle}{\sqrt{\langle h_1 | h_1 \rangle \langle h_2 | h_2 \rangle}}, \quad (32)$$

where the inner product is defined by

$$\langle h_1 | h_2 \rangle := 4R \int \frac{\tilde{h}_1(f) \tilde{h}_2^*(f)}{s_n(f)} df, \quad (33)$$

where the asterisk is a complex conjugate,  $\tilde{h}$  is the Fourier transform of  $h$ , and  $S_n$  is the noise power spectral density of the detector (which we take to be the sky-averaged LISA noise).

To simulate the evolving match found as observation time grows, only the first  $t$  units of time of  $h_1$  and  $h_2$  are considered. In this way, we are able to make the above fitting factor a function of observation time. In Fig. 5, we show a comparison for this mismatch when at resonance and when not at resonance. Per the KAM theorem, when off-resonance, the effect of the perturbation can almost be absorbed into shifting of fundamental frequencies. This confirms our understanding that these tidal perturbations need not be modeled for EMRI systems when off-resonance, given then planned sensitivity of LISA.

## C. Inspiral Times

As a rough estimate for the inspiral time, we use  $\tau_{\text{inspiral}} \sim -E/\langle P \rangle$ , where  $\langle P \rangle$  is the initial orbit-averaged

gravitational power radiated, and  $E$  is the initial energy of the system. For the power, one can use the quadrupole-octupole expansion as seen in Ref. [43]. However, this level of fidelity is unnecessary for our purposes. To obtain an order of magnitude estimate, we instead choose to use a result for circular Keplerian orbits. While this will lose accuracy for the power, the order of magnitude should be correct. We therefore use the result for a point mass in a Keplerian orbit with zero eccentricity [48],

$$\langle P \rangle = \frac{32}{5} \frac{G^4}{c^5} \frac{m_1^2 m_2^2 (m_1 + m_2)}{a^5}. \quad (34)$$

In our prescription of units,  $G = c = m_1 = 1$  and  $m_2 = q$  where  $q \ll 1$  is the mass ratio. We also use  $p$  (as defined in Eq. (8)) in place of  $a$  and expand in  $q \ll 1$ ,

$$\langle P \rangle \approx \frac{32}{5} \frac{q^2}{p^5}. \quad (35)$$

For the initial energy, we use the Hamiltonian for the system. We have up to this point been using the Hamiltonian per unit mass, i.e.,  $E = qH$ . Our final expression for inspiral time is then

$$\tau_{\text{inspiral}} \sim -\frac{5}{32} \frac{Hp^5}{q}. \quad (36)$$

#### D. Dephase Time

To quantify the necessity of modeling tidal effects, we will be comparing the above inspiral time to a dephase time. For our approximate analysis, this is a much simpler calculation than e.g. computing the phase jump accumulated when crossing a resonance [15]. Instead, we use a 95% match threshold to mark when the perturbed and unperturbed systems have “dephased” [47, 49, 50]. We take this value of the mismatch as a weak criterion, bearing in mind the limited accuracy of our simple approximate model, whose ingredients are only qualitatively correct [50]. Denoting this dephase time as  $\tau_{\text{dephase}}$ , we are interested in the realm of parameter space in which  $\tau_{\text{inspiral}} > \tau_{\text{dephase}}$ , since this is the realm in which the dephasing due to failing to properly model perturbations at resonance will produce detectable differences in waveforms.

This dephase time, however, requires some further consideration. This is because the exact time to reach the 95% threshold depends on the exact initial conditions within the resonance. This is made evident in Fig. 6, where significantly different dephase times can be found for the same magnitude of perturbation. Most notably, we can find arbitrarily long dephase times very near the hyperbolic points and near the elliptic points. We have observed consistent dephase times roughly halfway inside the elliptic region, and so we take this to be a characteristic dephase time of the resonance.

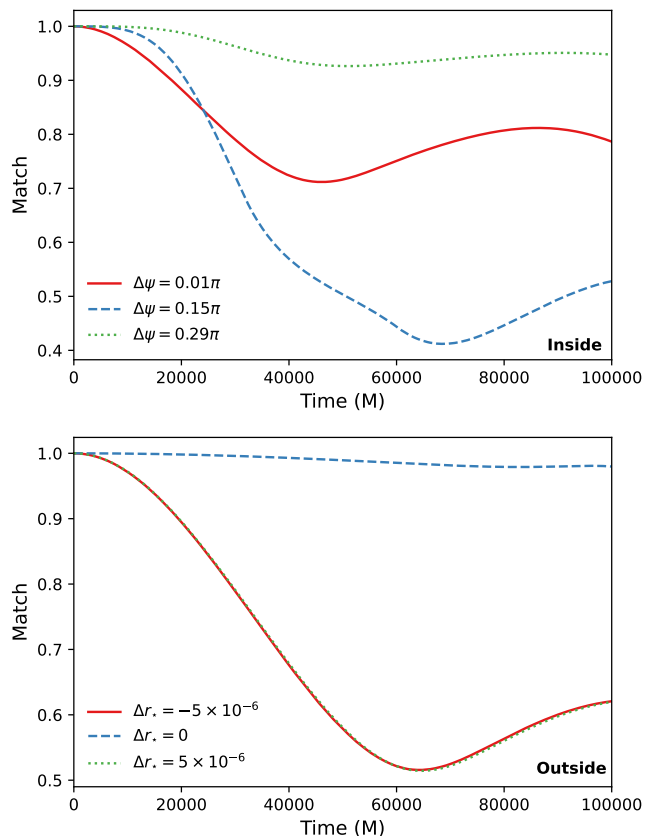


FIG. 6. Match comparison inside and outside of the elliptic region with a perturbation amplitude of  $\varepsilon = 10^{-7.5}$ . As expected, little dephasing is seen near the elliptic fixed point (dotted green line in top figure) or near the hyperbolic fixed point (dashed blue line in bottom figure). The most representative region of initial conditions (based on several more cases not shown here) is about half way inside the elliptic region (represented by the red line in the top figure).

#### E. Comparison

In the top panel of Fig. 7, we show dephase times found at several magnitudes of perturbation. However, most levels of perturbation were not thoroughly analyzed throughout the elliptic region. Most importantly, the dephase times were not taken consistently at a point midway into the elliptic region, and so there is more variance than would be desired. We nevertheless find a consistent trend of dephase times following a  $O(1/\sqrt{\varepsilon})$  power law, in agreement with analytical scaling arguments [39, 51]. Since we are confident in the power law relation, we elect to place a fit line based on  $\varepsilon = 10^{-7.5}$  only. We performed a more thorough search of the elliptic region at this  $\varepsilon$ , and it is where we found consistent dephase times midway into the elliptic region.

We estimate the inspiral times for various mass ratios using Eq. (36) and the results are presented in the bottom panel of Fig. 7. We see that at any given magnitude of perturbation, there is a critical mass ratio beyond which

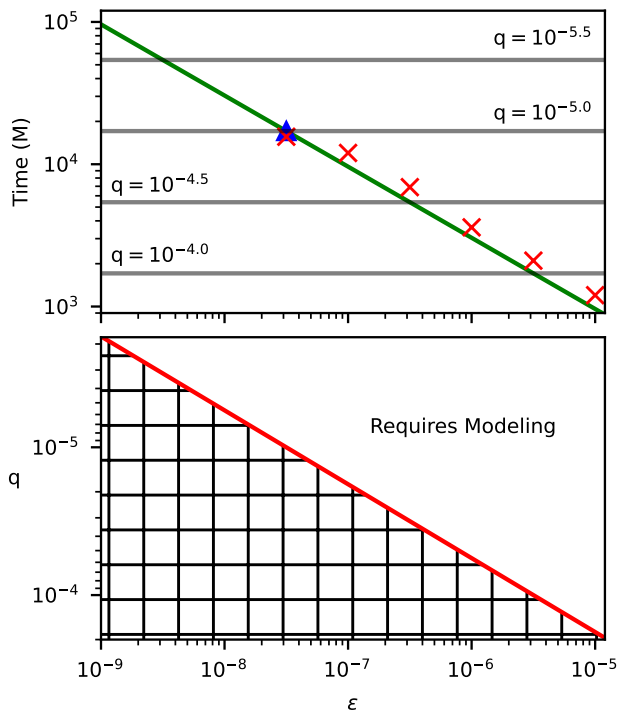


FIG. 7. Top: Dephasing time vs. perturbation level inside the elliptic region. Estimated inspiral times for various mass ratios are displayed as horizontal lines. Bottom: The critical curve where the effects of resonance breakdown become detectable. A full modeling scheme will be needed for perturbations at resonance for systems above the critical curve (with larger perturbation or more extreme mass ratios).

tidal perturbations must be modeled. A more succinct visual description of the region that requires modeling can be found in the bottom panel of Fig. 7. This figure shows the critical mass ratio as a function of perturbation strength, and highlights the fact that perturbations must be modeled for more extreme mass ratios.

## VII. DISCUSSION AND CONCLUSIONS

Using a Newtonian analogue of a Kerr black hole, we performed a preliminary analysis of the effect of an external tidal field on EMRI systems. While such effects have been previously studied, the unique impact tidal perturbations have when a system is at resonance has not been thoroughly explored. We qualitatively explored some issues in the case of perturbed resonances, such as the impact of entry point into the resonance, and we found an approximate threshold for which further modeling will be necessary.

In our analysis, we used two measures to study this effect: the fitting factor between waveforms from the perturbed and unperturbed systems; and the evolution of the resonance angle for the perturbed system. Both ap-

proaches proved valuable in understanding how detection of EMRI systems will be impacted by tidal perturbations. The analysis of dephasing times reveals a broad region of parameter space for which the characteristic time scale of the tidal perturbation at resonance (the dephasing time) is shorter than the inspiral time. In this region of parameter space, proper modeling of the tidal perturbation will be necessary to accurately model the waveform. This space is shown in Fig. 7. Our analysis indicates this region of parameter space is approximately

$$\varepsilon \gtrsim 300 q^2, \quad (37)$$

where  $q = m/M \ll 1$  is the mass ratio and  $\varepsilon \ll 1$  is a dimensionless scalar quantity indicating the strength of the tidal force. For an external perturber of mass  $M_*$  at a distance  $d$ ,  $\varepsilon = M^2 M_*/d^3$ .

In addition to an estimated range for which the tidal resonance effects are relevant, we also found that different entry points into resonance can produce substantially different dynamics. This can be best seen in Figure 4. If entering near the hyperbolic point, the resonance angle can evolve arbitrarily slowly. This is in contrast to entering between hyperbolic points where the resonance angle varies most quickly. A dependence between the entry point and the dynamics of the system was also reported when studying a non-Kerr solution [16] in the adiabatic approximation.

To improve our understanding of these systems, future work is needed which simultaneously uses the Kerr spacetime, includes radiation reaction, and a tidal perturbation. With such a model, the region of parameter space for which tidal perturbations are important could be narrowed and account for more parameters, e.g. eccentricity and inclination, different orbital resonances, and alignment of the tidal force. Such work could help in constructing a robust model for traversing resonances [15], able to account for the changes to phase space due to an arbitrary tidal force.

We found that this Newtonian analogue is a good compromise between a system complex enough to exhibit resonant effects, and still simple enough to be numerically and analytically tractable. Our results present another example (e.g., see Refs. [52–54]) where the use of an analogue provides insight and motivates targeted studies in the full system.

The LISA mission’s capacity to probe strong gravity with EMRIs depends on the ongoing endeavors to build precise GW models for these systems. Extending the breadth of this study to the morphology and characteristic of these prolonged resonances could reveal when general resonant phenomena must be included to properly model EMRIs. If these effects are not accounted for, they could lead to incorrect parameter estimation or fundamental biases when testing general relativity.

## ACKNOWLEDGMENTS

We would like to thank J. Meyer for useful discussions and comments, and E. Flanagan and S. Hughes for valuable feedback on an earlier draft of this paper. A.C.-A. acknowledges funding from the Fundación Universitaria Konrad Lorenz (Project 5INV1), from Will and Kacie Snellings, and thanks the Department of Physics at the University of Mississippi, where part of this work

was performed, for their hospitality. Some of the computational efforts presented here were performed on the Scientific Computing Laboratory, operated and supported by Fundación Universitaria Konrad Lorenz's Engineering and Mathematics Department. L.C.S. acknowledges D. Nichols and K. Deck for helpful discussions. The work of L.C.S. was partially supported by NSF CAREER Award PHY-2047382. In preparing this manuscript we made use of the `python` packages `numpy` [55], `scipy` [32], and `matplotlib` [56].

- 
- [1] E. Barausse *et al.*, Prospects for Fundamental Physics with LISA, *Gen. Rel. Grav.* **52**, 81 (2020), [arXiv:2001.09793 \[gr-qc\]](#).
- [2] S. Babak, J. Gair, A. Sesana, E. Barausse, C. F. Sopuerta, C. P. L. Berry, E. Berti, P. Amaro-Seoane, A. Petiteau, and A. Klein, Science with the space-based interferometer LISA. V: Extreme mass-ratio inspirals, *Phys. Rev. D* **95**, 103012 (2017), [arXiv:1703.09722 \[gr-qc\]](#).
- [3] V. Vázquez-Aceves, L. Zwick, E. Bortolas, P. R. Capelo, P. Amaro-Seoane, L. Mayer, and X. Chen, Revised event rates for extreme and extremely large mass-ratio inspirals, [arXiv:2108.00135 \[astro-ph.GA\]](#).
- [4] L. V. Drummond and S. A. Hughes, Precisely computing bound orbits of spinning bodies around black holes I: General framework and results for nearly equatorial orbits, [arXiv:2201.13334 \[gr-qc\]](#).
- [5] B. Carter, Global structure of the Kerr family of gravitational fields, *Phys. Rev.* **174**, 1559 (1968).
- [6] W. Schmidt, Celestial mechanics in Kerr space-time, *Class.Quant.Grav.* **19**, 2743 (2002), [arXiv:gr-qc/0202090 \[gr-qc\]](#).
- [7] S. Drasco and S. A. Hughes, Rotating black hole orbit functionals in the frequency domain, *Phys. Rev. D* **69**, 044015 (2004), [arXiv:astro-ph/0308479](#).
- [8] G. Contopoulos, *Order and Chaos in Dynamical Astronomy* (Springer Berlin Heidelberg, Berlin, Heidelberg, 2002) oCLC: 851375749.
- [9] V. I. Arnol'd, *Mathematical methods of classical mechanics*, Vol. 60 (Springer-Verlag New York, 1978).
- [10] Y. Mino, M. Sasaki, and T. Tanaka, Gravitational radiation reaction to a particle motion, *Phys. Rev. D* **55**, 3457 (1997), [arXiv:gr-qc/9606018](#).
- [11] T. C. Quinn and R. M. Wald, An Axiomatic approach to electromagnetic and gravitational radiation reaction of particles in curved space-time, *Phys. Rev. D* **56**, 3381 (1997), [arXiv:gr-qc/9610053](#).
- [12] S. A. Hughes, S. Drasco, E. E. Flanagan, and J. Franklin, Gravitational radiation reaction and inspiral waveforms in the adiabatic limit, *Phys. Rev. Lett.* **94**, 221101 (2005), [arXiv:gr-qc/0504015](#).
- [13] U. Ruangsri and S. A. Hughes, Census of transient orbital resonances encountered during binary inspiral, *Phys. Rev. D* **89**, 084036 (2014), [arXiv:1307.6483 \[gr-qc\]](#).
- [14] E. E. Flanagan and T. Hinderer, Transient resonances in the inspirals of point particles into black holes, *Phys. Rev. Lett.* **109**, 071102 (2012), [arXiv:1009.4923 \[gr-qc\]](#).
- [15] P. Gupta, B. Bonga, A. J. K. Chua, and T. Tanaka, Importance of tidal resonances in extreme-mass-ratio inspirals, *Phys. Rev. D* **104**, 044056 (2021), [arXiv:2104.03422 \[gr-qc\]](#).
- [16] G. Lukes-Gerakopoulos, T. A. Apostolatos, and G. Contopoulos, Observable signature of a background deviating from the Kerr metric, *Phys. Rev. D* **81**, 124005 (2010), [arXiv:1003.3120 \[gr-qc\]](#).
- [17] A. Cárdenas-Avedaño, A. F. Gutierrez, L. A. Pachón, and N. Yunes, The exact dynamical Chern–Simons metric for a spinning black hole possesses a fourth constant of motion: A dynamical-systems-based conjecture, *Class. Quant. Grav.* **35**, 165010 (2018), [arXiv:1804.04002 \[gr-qc\]](#).
- [18] G. Lukes-Gerakopoulos and V. Witzany, Non-linear effects in EMRI dynamics and their imprints on gravitational waves, in *Handbook of Gravitational Wave Astronomy*, edited by C. Bambi, S. Katsanevas, and K. D. Kokkotas (Springer, Singapore, 2021) [arXiv:2103.06724 \[gr-qc\]](#).
- [19] K. Destounis, A. G. Suvorov, and K. D. Kokkotas, Gravitational-wave glitches in chaotic extreme-mass-ratio inspirals, *Phys. Rev. Lett.* **126**, 141102 (2021), [arXiv:2103.05643 \[gr-qc\]](#).
- [20] H. Yang and M. Casals, General Relativistic Dynamics of an Extreme Mass-Ratio Binary interacting with an External Body, *Phys. Rev. D* **96**, 083015 (2017), [arXiv:1704.02022 \[gr-qc\]](#).
- [21] B. Bonga, H. Yang, and S. A. Hughes, Tidal resonance in extreme mass-ratio inspirals, *Phys. Rev. Lett.* **123**, 101103 (2019), [arXiv:1905.00030 \[gr-qc\]](#).
- [22] C. P. L. Berry, R. H. Cole, P. Cañizares, and J. R. Gair, Importance of transient resonances in extreme-mass-ratio inspirals, *Phys. Rev. D* **94**, 124042 (2016), [arXiv:1608.08951 \[gr-qc\]](#).
- [23] L. Speri and J. R. Gair, Assessing the impact of transient orbital resonances, *Phys. Rev. D* **103**, 124032 (2021), [arXiv:2103.06306 \[gr-qc\]](#).
- [24] C. M. Will, Carter-like constants of the motion in Newtonian gravity and electrodynamics, *Phys. Rev. Lett.* **102**, 061101 (2009), [arXiv:0812.0110 \[gr-qc\]](#).
- [25] K. Glampedakis and T. Apostolatos, The separable analogue of Kerr in Newtonian gravity, *Class. Quant. Grav.* **30**, 055006 (2013), [arXiv:1301.3309 \[gr-qc\]](#).
- [26] A. Eleni and T. A. Apostolatos, A Newtonian analogue of Kerr black hole, *Phys. Rev. D* **101**, 044056 (2019), [arXiv:1912.03499 \[gr-qc\]](#).
- [27] J. P. Vinti, Invariant Properties of the Spheroidal Potential of an Oblate Planet, *Journal of Research of the National Bureau of Standards* **70**, 1 (1966).
- [28] Y. Mino, Perturbative approach to an orbital evolution around a supermassive black hole, *Phys. Rev. D* **67**, 084027 (2003), [arXiv:gr-qc/0302075](#).

- [29] C. Misner, K. Thorne, and J. Wheeler, *Gravitation* (W. H. Freeman, San Francisco, 1973).
- [30] R. Emami and A. Loeb, Detectability of Gravitational Wave from a population of Inspiralling Black Holes in Milky Way Mass Galaxies, [arXiv:1903.02579 \[astro-ph.HE\]](#).
- [31] H. Yoshida, Construction of higher order symplectic integrators, *Phys. Lett. A* **150**, 262 (1990).
- [32] P. Virtanen, R. Gommers, T. E. Oliphant, M. Haberland, T. Reddy, D. Cournapeau, E. Burovski, P. Peterson, W. Weckesser, J. Bright, S. J. van der Walt, M. Brett, J. Wilson, K. J. Millman, N. Mayorov, A. R. J. Nelson, E. Jones, R. Kern, E. Larson, C. J. Carey, Í. Polat, Y. Feng, E. W. Moore, J. VanderPlas, D. Laxalde, J. Perktold, R. Cimrman, I. Henriksen, E. A. Quintero, C. R. Harris, A. M. Archibald, A. H. Ribeiro, F. Pedregosa, P. van Mulbregt, and SciPy 1.0 Contributors, SciPy 1.0: Fundamental Algorithms for Scientific Computing in Python, *Nature Methods* **17**, 261 (2020).
- [33] V. I. Arnold, *Ordinary differential equations*, Universitext (Springer-Verlag, Berlin, 2006) pp. ii+334, translated from the Russian by Roger Cooke, Second printing of the 1992 edition.
- [34] H. Poincaré, Sur le problème des trois corps et les équations de la dynamique, *Acta mathematica* **13**, A3 (1890).
- [35] P. Patsis and L. Zachilas, Using color and rotation for visualizing four-dimensional Poincaré cross-sections: With applications to the orbital behavior of a three-dimensional hamiltonian system, *International Journal of Bifurcation and Chaos* **4**, 1399 (1994).
- [36] L. Zachilas, M. Katsanikas, and P. A. Patsis, The structure of phase space close to fixed points in a 4D symplectic map, *Chaos Solitons Fractals* **23**, 1330023 (2013), [arXiv:1205.4575 \[nlin.CD\]](#).
- [37] M. Richter, S. Lange, A. Bäcker, and R. Ketzmerick, Visualization and comparison of classical structures and quantum states of four-dimensional maps, *Phys. Rev. E* **89**, 022902 (2014), [arXiv:1307.6109 \[nlin.CD\]](#).
- [38] G. Lukes-Gerakopoulos, M. Katsanikas, P. A. Patsis, and J. Seyrich, The dynamics of a spinning particle in a linear in spin Hamiltonian approximation, *Phys. Rev. D* **94**, 024024 (2016), [arXiv:1606.09171 \[gr-qc\]](#).
- [39] V. I. Arnold, V. V. Kozlov, and A. I. Neishtadt, *Mathematical aspects of classical and celestial mechanics* (Springer-Verlag, Berlin, 1997) pp. xiv+291, translated from the 1985 Russian original by A. Iacob, Reprint of the original English edition from the series Encyclopaedia of Mathematical Sciences [it Dynamical systems. III, Encyclopaedia Math. Sci., 3, Springer, Berlin, 1993; MR1292465 (95d:58043a)].
- [40] M. van de Meent, Conditions for Sustained Orbital Resonances in Extreme Mass Ratio Inspirals, *Phys. Rev. D* **89**, 084033 (2014), [arXiv:1311.4457 \[gr-qc\]](#).
- [41] C. D. Murray and S. F. Dermott, *Solar System Dynamics* (Cambridge University Press, 1998).
- [42] J. R. Gair and K. Glampedakis, Improved approximate inspirals of test-bodies into Kerr black holes, *Phys. Rev. D* **73**, 064037 (2006), [arXiv:gr-qc/0510129](#).
- [43] S. Babak, H. Fang, J. R. Gair, K. Glampedakis, and S. A. Hughes, 'Kludge' gravitational waveforms for a test-body orbiting a Kerr black hole, *Phys. Rev. D* **75**, 024005 (2007), [Erratum: *Phys. Rev. D* **77**, 04990 (2008)], [arXiv:gr-qc/0607007](#).
- [44] C. F. Sopuerta and N. Yunes, Extreme and Intermediate-Mass Ratio Inspirals in Dynamical Chern-Simons Modified Gravity, *Phys. Rev. D* **80**, 064006 (2009), [arXiv:0904.4501 \[gr-qc\]](#).
- [45] K. S. Thorne, Multipole Expansions of Gravitational Radiation, *Rev. Mod. Phys.* **52**, 299 (1980).
- [46] A. J. K. Chua, C. J. Moore, and J. R. Gair, Augmented kludge waveforms for detecting extreme-mass-ratio inspirals, *Phys. Rev. D* **96**, 044005 (2017), [arXiv:1705.04259 \[gr-qc\]](#).
- [47] C. Cutler and E. E. Flanagan, Gravitational waves from merging compact binaries: How accurately can one extract the binary's parameters from the inspiral wave form?, *Phys. Rev. D* **49**, 2658 (1994), [arXiv:gr-qc/9402014](#).
- [48] P. C. Peters and J. Mathews, Gravitational Radiation from Point Masses in a Keplerian Orbit, *Phys. Rev.* **131**, 435440 (1963).
- [49] E. E. Flanagan and S. A. Hughes, Measuring gravitational waves from binary black hole coalescences: 2. The Waves' information and its extraction, with and without templates, *Phys. Rev. D* **57**, 4566 (1998), [arXiv:gr-qc/9710129](#).
- [50] K. Glampedakis and S. Babak, Mapping spacetimes with LISA: Inspiral of a test-body in a 'quasi-Kerr' field, *Class. Quant. Grav.* **23**, 4167 (2006), [arXiv:gr-qc/0510057](#).
- [51] V. I. Arnold, Applicability conditions and an error bound for the averaging method for systems in the process of evolution through a resonance, *Dokl. Akad. Nauk SSSR* **161**, 9 (1965); A. B. Givental, B. A. Khesin, J. E. Marsden, A. N. Varchenko, V. A. Vassiliev, O. Y. Viro, and V. M. Zakalyukin, eds., Conditions for the applicability, and estimate of the error, of an averaging method for systems which pass through states of resonance in the course of their evolution, in *Collected Works: Representations of Functions, Celestial Mechanics and KAM Theory, 1957–1965* (Springer Berlin Heidelberg, Berlin, Heidelberg, 2009) pp. 477–480.
- [52] W. G. Unruh, Experimental black hole evaporation, *Phys. Rev. Lett.* **46**, 1351 (1981).
- [53] M. W. Ray, E. Ruokokoski, S. Kandel, M. Möttönen, and D. S. Hall, Observation of Dirac monopoles in a synthetic magnetic field, *Nature* **505**, 657 (2014), [arXiv:1408.3133 \[cond-mat.quant-gas\]](#).
- [54] T. Torres, S. Patrick, A. Coutant, M. Richartz, E. W. Tedford, and S. Weinfurter, Observation of superradiance in a vortex flow, *Nature Phys.* **13**, 833 (2017), [arXiv:1612.06180 \[gr-qc\]](#).
- [55] C. R. Harris, K. J. Millman, S. J. van der Walt, R. Gommers, P. Virtanen, D. Cournapeau, E. Wieser, J. Taylor, S. Berg, N. J. Smith, R. Kern, M. Picus, S. Hoyer, M. H. van Kerkwijk, M. Brett, A. Haldane, J. F. del Río, M. Wiebe, P. Peterson, P. Gérard-Marchant, K. Sheppard, T. Reddy, W. Weckesser, H. Abbasi, C. Gohlke, and T. E. Oliphant, Array programming with NumPy, *Nature* **585**, 357 (2020).
- [56] J. D. Hunter, Matplotlib: A 2d graphics environment, *Computing in Science & Engineering* **9**, 90 (2007).